CeO_2 Nanorods Supported M–Co Bimetallic Oxides (M=Fe, Ni, Cu) for Catalytic CO and C_3H_8 Oxidation

Zhongqi Liu,[1] Junhao Li[1] and Ruigang Wang[1]*

[1]*Department of Metallurgical and Materials Engineering, The University of Alabama, Tuscaloosa, AL 35487, United States*

ABSTRACT

Supported bimetallic catalysts with rational compositions and structural design have attracted great interest, due to the tunable structural orientation (alloy or intermetallic compound and core-shell structure etc.), synergetic effects, and combined properties related to the presence of two individual metals. In this study, 10 wt% Fe-Co, Ni-Co and Cu-Co bimetallic oxides with 1:2 atomic ratio ($FeCo_2O_x$, $NiCo_2O_x$ and $CuCo_2O_x$) were deposited onto CeO_2 nanorods (CeO_2NR) via a hydrothermal-assisted precipitation-deposition method. The bimetallic synergism effects, surface structure configuration and the metal (oxide)-support interactions were investigated. The catalysts were characterized by means of powder XRD, TEM, EDX, Raman spectroscopy, XPS, BET surface area, H_2-TPR, O_2 pulse chemisorption and O_2-TPD. All the CeO_2NR supported bimetallic catalysts show considerable low-temperature CO oxidation performance. And the catalytic activity toward CO oxidation follows the order: 10 wt% $CuCo_2O_x/CeO_2NR$ (T_{50}= 95 °C and T_{90}= 148 °C) > 10 wt% $FeCo_2O_x/CeO_2NR$ (T_{50}= 129 °C and T_{90}= 193 °C) > 10 wt% $NiCo_2O_x/CeO_2NR$ (T_{50}= 147 °C and T_{90}= 196 °C). As for the catalytic oxidation of C_3H_8, all the designed catalysts show similar low-temperature performance, but the 10 wt% $NiCo_2O_x/CeO_2NR$ catalyst exhibits the maximum C_3H_8 conversion above 330 °C. In addition, we also demonstrate the important role of oxygen storage capacity (OSC) and the impact of different oxygen species (physi-/chemisorbed oxygen, and bulk lattice oxygen) on the oxidation of CO and light hydrocarbons.

Keywords: CO and C_3H_8 oxidation; Bimetallic synergism; Cobalt catalysts; Support effect

1. INTRODUCTION

Monometallic and bimetallic catalysts with ceria (CeO_2) as support or promoter have been widely investigated due to CeO_2's remarkable redox activity [1-3], oxygen storage/release capacity [4-6], as well as facile surface oxygen mobility [7-9]. Along with the development of shape-controlled synthesis, CeO_2 with well-defined morphology, particularly CeO_2 nanorods (CeO_2NR), further becomes the focus of many supported catalyst research by virtue of its superior low temperature surface oxygen release ability and strong interactions with metal catalysts (i.e., clusters trapping and anchoring). It has been well documented that CeO_2NR possess a great number of surface-bound defects [10], i.e. oxygen vacancies or Ce^{3+} species as active sites [11], and expose more reactive facets {110}/{100} [12], although recently defect-rich {111} crystal plane was also observed on the surface of CeO_2NR [13-15]. In addition, CeO_2NR has been found to advance the dispersion of supported active species and promote the thermal stability of catalyst nanoclusters, both of which favor the low temperature catalytic activity and durability [16-18]. For instance, Lin et al. reported better water-gas shift (WGS) performance over Au/CeO_2 nanorods than Au/CeO_2 nanocubes, owing to the strong adhesion of Au to CeO_2NRsupport in the WGS reaction [19]. Cui and Dai also reported that Cu supported on CeO_2NR presents better activity for carbonate hydrogenation than Cu on CeO_2 nanocubes and nanopolyhedra [20].

Cobalt-based monometallic and bimetallic catalysts (cobalt oxides or FCC/HCP metallic cobalt) have been greatly acknowledged as efficient catalysts for environmental remediation [21-24], oxygen evolution reaction [25], fine chemical synthesis [26], and lately as an excellent cathode catalyst for Li–O_2 batteries [27]. In spite of monometallic Co_3O_4 catalysts being very catalytically active, various tentative approaches involving doping, alloying or hybrid catalysts have been applied to modify the nanostructure of Co_3O_4 to further promote its catalytic activity. Ma et al. [28] synthesized an indium-doped Co_3O_4 nanorod catalyst and demonstrated its enhanced performance on catalytic oxidation of CO and C_3H_6 in comparison with individual Co_3O_4 and In_2O_3 nanorod samples, and physical mixture sample of Co_3O_4 and In_2O_3. They also revealed that the addition of indium cation distorts the lattice structure of Co_3O_4, thus leading to the formation of high concentration surface oxygen vacancies. Zhou et al. [29] prepared a series of Cu doped Co_3O_4 nanowire with different amounts of Cu addition, and claimed that replacing the inactive Co^{2+} with more active Cu^{2+} cation which has similar ionic radius (Co^{2+}: 0.58 Å and Cu^{2+}: 0.57 Å) can lead to higher catalytic activity for CO oxidation. And according to the DFT calculation, they further demonstrated that the Cu substitution only slightly affects the CO adsorption energies but considerably decreases the oxygen vacancy formation energies. Similar phenomenon was also reported on the spinel $M_xCo_{3-x}O_4$ nanoarray catalysts developed by Ren et al. [30] In their work, controlled substitution of Co cation by Ni and Zn can manipulate the adsorption-desorption behavior and generate more surface oxygen defects, therefore presenting tunable low-temperature CH_4 and CO catalytic oxidation performance. In addition, Binder et al. [31] even presented a ternary mixed oxide CuO-Co_3O_4-CeO_2 catalyst with both low-temperature CO oxidation capability and high resistance to hydrocarbon inhibition. In the literature, the behavior and underlying mechanism of this catalytic system especially for the interaction between the cobalt-based bimetallic catalysts and CeO_2NR support has not been well studied. Inspired by the merits from the rod-shaped CeO_2 nanostructure and earlier studies on the catalytically active Co_3O_4-based single and binary oxides, in this work, we fabricated CeO_2NR supported Co_3O_4-based bimetallic (M-Co: M=Fe, Ni and Cu) oxides catalysts and studied the synergistic effect between Co and the second transition-metal cation (Fe, Ni and Cu).

Herein, we deposited 10 wt% Fe-Co, Ni-Co and Cu-Co bimetallic oxides with 1:2 atomic ratio (M:Co=1:2, M=Fe, Ni and Cu) onto CeO_2NR via a hydrothermal-assisted precipitation-deposition method, which were denoted as 10 wt% $FeCo_2O_x/CeO_2$NR, 10 wt% $NiCo_2O_x/CeO_2$NR and 10 wt.% $CuCo_2O_x/CeO_2$NR, and investigated their activity toward carbon monoxide (CO) and propane (C_3H_8) oxidation reactions. Meanwhile, monometallic 10 wt% Co_3O_4/CeO_2NR was also prepared and characterized for comparison purposes. The role of M-Co (M = Fe, Ni and Cu) synergism and metal-support interactions on the CO and C_3H_8 oxidation reactions are discussed.

2. EXPERIMENTAL SECTION

2.1 Catalysts Preparation

Chemicals. All of the chemicals used in this work were of analytical grade and purchased from Acros Organics without further purification.

Synthesis of CeO_2NR Support. CeO_2NR support was synthesized through a facile hydrothermal method [32]. Briefly, 8 mL aqueous NaOH solution (6 M) was added dropwise to a 200 mL Teflon-lined autoclave which contained 88 mL $Ce(NO_3)_3 \cdot 6H_2O$ solution (0.1 M) and the mixture was stirred for 15 s. The hydrothermal reaction procedure was carried out in a programmable box furnace at 90 °C for 48 h. After the autoclave was cooled down to room temperature, the precipitates were collected, and then washed with deionized water (500 mL) and ethanol (50 mL). The as-prepared samples were obtained by drying in an oven at 60 °C overnight.

Fabrication of 10 wt% $M_xCo_{3-x}O_4/CeO_2NR$ (M = Fe, Ni, Cu). In a typical procedure, 0.9 g of the as-prepared CeO_2NR were first suspended in 96 mL of ethanol and 4 mL of deionized water under magnetic stirring. Then, $Cu(OAc)_2{\cdot}H_2O$ (0.1100 g) and $Co(OAc)_2{\cdot}4H_2O$ (0.2747 g) were dissolved in the suspension above. During the process, 0.5 mL aqueous ammonium hydroxide was added dropwise into the mixture. After further aged at 80 °C for 20 h, the reaction mixture was transferred into a 200 mL autoclave for hydrothermal reaction at 150 °C for 1 h. After the autoclave cooled down to room temperature, the resulting mixture was transferred to a beaker and kept in a drying oven at 80 °C for 24 h to obtain the dry powder. Finally, the as-prepared powder was calcined in a box furnace at 400 °C for 5 h to obtain the sample 10 wt% $CuCo_2O_x/CeO_2NR$. Similarly, 10 wt% $FeCo_2O_x/CeO_2NR$ was prepared by using $Fe(NO_3)_3{\cdot}9H_2O$ (0.2322 g) and $Co(OAc)_2{\cdot}4H_2O$ (0.2869 g), and 10 wt% $NiCo_2O_x/CeO_2NR$ was obtained by adding $Ni(NO_3)_2{\cdot}6H_2O$ (0.1645 g) and $Co(OAc)_2{\cdot}4H_2O$ (0.2821 g). For comparison, 10 wt% Co_3O_4/CeO_2NR were prepared with adding $Co(OAc)_2{\cdot}4H_2O$ solely.

2.2 Characterization of Catalysts

Powder X-ray diffraction (XRD) of the samples was recorded on a Philips X'Pert MPD with Cu Kα radiation source (λ: 1.5405 Å) operating at 45 kV and 40 mA. The data was collected in a 2θ range from 10° to 90°, with a scanning rate of 0.005°/s. The crystalline phases were indexed according to the powder XRD database (JCPDS-ICDD). The recorded patterns were analyzed using JADE 6.0 software to obtain lattice constants and average crystallite sizes based on the Scherrer equation.

Raman spectra were acquired using a Horiba LabRAM HR 800 Raman spectrometer in the spectral window from 100 to 1200 cm^{-1}. Diode-Pumped Solid-State (DPSS) laser system (Laser Quantum MPC6000) tuned at λ=532 nm was used for excitation. The ×100 LWD objective (LWD: long working distance; NA (numerical aperture) = 0.6, 1% filtering optics, 50 s of exposure time and 10 accumulation numbers were used for measuring all the samples. All Raman spectra were calibrated using a silicon single crystal wafer as the reference (520.7 cm^{-1}) and analyzed to obtain the elemental coordination environment and concentration of defect sites.

X-ray photoelectron spectroscopy (XPS) was carried out by a Kratos Axis Ultra DLD spectrometer using Al Kα radiation under ultra-high vacuum (UHV) conditions, which had a base pressure of 10^{-10} Torr. The photoelectron emission spectra were recorded using an Al-Kα (hν = 1486.6 eV). The carbonaceous C 1s line (284.4 eV) was used as an internal standard to calibrate the binding energies. The spectra were analyzed using CasaXPS software.

The particle morphologies and sizes of the as-prepared samples were examined with a transmission electron microscope (TEM, FEI Tecnai F20), which was operated at 200 kV, equipped with a high angle annular dark field (HAADF) detector and EDAX energy dispersive X-ray system. All of the investigated powder samples were sonicated in ethanol for 10 min and then deposited onto an ultrathin carbon coated Cu grid (from Ted Pella) using a glass pipette.

Single point BET surface area of the catalysts was determined by N_2 adsorption/desorption isotherms at liquid nitrogen temperature (-196 °C). Hydrogen temperature programmed reduction (H_2-TPR) was performed using a Micrometrics AutoChem II 2920 with the temperature rising from 30 to 900 °C. The gas mixture of 10 vol.% H_2 and 90 vol.% Ar passed through the different samples (~90 mg) with a flowing rate of 50 mL/min. Standard silver oxide (Ag_2O) sample was used for the H_2-TPR calibration in order to calculate H_2 consumption.

Oxygen temperature-programmed desorption (O_2-TPD) was conducted using the same instrument as H_2-TPR to investigate the interaction of O_2 with the catalyst surface. The powder sample in U-tube was heated from 30 to 400 °C under a helium stream (50 mL/min) to remove residual moisture. After the sample was cooled to 30 °C, 5 vol.% O_2 - 95 vol.% He gas mixture was flowed at 50 mL/min through the sample for 60 min. Finally, the sample was heated up to 800 °C again under helium gas and the desorption behavior of different O_2 species can be monitored by a TCD detector at elevated temperatures.

Carbon monoxide temperature-programmed desorption (CO-TPD) was conducted using the same Micrometrics AutoChemTM II 2920 chemisorption analyzer. ~50 mg powder sample in U-tube was heated from room temperature to 400 °C under a Helium stream (50 mL/min) to remove residual moisture. After the sample was cooled to room temperature, the mixture of 10 vol% CO/90 vol% He gas was flowed at 50 mL/min through the sample for 60 min. Finally, the sample was heated up to 400 °C again under Helium gas flow and the desorption behavior of CO species was monitored by a TCD detector at elevated temperature.

The oxygen storage capacity of the samples was performed on the same AutoChem II 2920 instrument. Generally, 30 mg sample was initially pretreated from 30 to 550 °C under a 10 vol.% H_2-Ar flow (50 mL/min) and kept at 550 °C for 30 min. Then the sample was cooled down to 200 °C with He (50 mL/min) flow, and the system was purged until the baseline established. Subsequently, 0.48 mL of 5 vol.% O_2/He was injected into the reactor at 200 ℃ every 1.5 min in the He carrier gas (50 mL/min) until the saturated adsorption of O_2 was reached. The complete oxygen storage capacity complete (OSCC) was determined by total consumption during the O_2 pulse.

2.3 Catalytic Evaluation

CO oxidation activity of the catalysts was carried out in a downward and fixed-bed plugged quartz tubular reactor system, loaded with 50 mg of the catalyst dispersed over quartz wool. No pretreatment was applied before the catalytic activity test. The reaction gas, a mixture of 1 vol.%

CO with 20 vol.% O_2 and 79 vol.% He was fed over the catalyst at a flow rate of 38 mL/min corresponding to a Weight Hour Space Velocity (WHSV) value of 46,000 $mLh^{-1}g_{cat}^{-1}$. The outlet gas was analyzed by a gas chromatograph (SRI multiple gas analyzer GC) equipped with a thermal conductivity detector (TCD). The CO conversion was calculated according to the equation:

$$\mathrm{CO\ conversion\ (\%)} = \frac{X_{\mathrm{CO_2}}}{X_{\mathrm{CO_2}} + X_{\mathrm{CO}}} \times 100\%$$

where X_{CO} and X_{CO2} are the partial pressure of CO and CO_2, respectively, which are determined from the relative peak area of the CO and CO_2 peaks normalized to the He standard.

The C_3O_8 oxidation reaction was also used to evaluate the catalysts activity with a similar fixed-bed apparatus. 50 mg of the catalyst was loaded into the quartz reactor, and the reaction gas fed was consisted of 0.2 vol.% C_3H_8, 2.0 vol.% O_2 and N_2 balance with a flow rate of 30 mL/min. The conversion of C_3H_8 was measured before and after the catalytic reaction by an online gas chromatograph (SRI multiple gas analyzer GC) with TCD detector. The C_3H_8 conversion ($X_{\mathrm{C_3H_8}}$) was calculated using the following equation:

$$X_{\mathrm{C_3H_8}}\ (\%) = \frac{[\mathrm{C_3H_8}]_{\mathrm{in}} - [\mathrm{C_3H_8}]_{\mathrm{out}}}{[\mathrm{C_3H_8}]_{\mathrm{in}}} \times 100\%$$

where $[C_3H_8]_{in}$ and $[C_3H_8]_{out}$ are the concentration of C_3H_8 in the influent and effluent gas flow.

3. RESULTS AND DISCUSSION

3.1 Morphology and structural description

The actual loading content of Co and the second transition-metal cation M (M=Fe, Ni or Cu) was determined by EDS analysis and the atomic ratio of Co to M is presented in Table 1, which is conformed to the initial adding amount. In Figure 1(a), all the XRD patterns display the diffraction peaks of cubic fluorite CeO_2 phase (JCPDS# 34-0394, space group Fm3m), indicating that three cobalt-based bimetallic oxides species are all supported on the CeO_2NR matrix. Figure 1(b) shows the enlarged regions of the XRD patterns in Figure 1(a) from 2θ =33.5° to 45°, in which the most intense (311) reflection arising from cobalt (II, III) oxide (Co_3O_4, JCPDS# 71-0816, space group F-43m) can be observed in all CeO_2NR supported Fe-Co, Ni-Co and Cu-Co bimetallic samples. And compared with monometallic 10% Co_3O_4/CeO_2NR sample, the intensity of cobalt (II, III) oxide (311) diffraction decreases due to the incorporation of the second transition metal M (M = Fe, Ni or Cu). The crystallite size was estimated by Scherrer equation based on X-ray line broadening of the (111) reflection profile of CeO_2 (see Table 1), and no significant differences can be noted in these catalysts. However, it needs to be pointed out that the lattice constant of CeO_2NR support reduces significantly, in contrast to pure CeO_2NR with a reported lattice constant of 5.4142 Å [33]. The reduction of the lattice constant can be explained by the substitution of the smaller Co/Fe/Ni/Cu ions for Ce^{4+} ions (Co^{2+}: 0.58 Å, Fe^{2+}: 0.63 Å, Ni^{2+}: 0.55 Å, Cu^{2+}: 0.57 Å and Ce^{4+}: 0.97 Å), thus shrinking the CeO_2 unit cell [34-36]. For comparison, the lattice constant of 10 wt% Co_3O_4/CeO_2NR is 5.4116 Å, which is a little smaller than that of CeO_2NR. Apart from this, the formation of N-O-Ce (N=Co, Fe, Cu, or Ni) solid solution on CeO_2NR surface can reduce the lattice constant of CeO_2 as well [33, 37]. In any case, the metal(oxide)-support interaction by cation diffusion and/or substitution was confirmed between cobalt-based bimetallic oxides and CeO_2NR support.

The cation coordination environment and defect structure (i.e., oxygen vacancy concertation) of the catalysts were characterized using Raman spectroscopy. Figure 2a shows the Raman spectra of CeO_2NR supported MCo_2O_x (M=Fe, Ni and Cu) bimetallic catalysts and pure CeO_2NR support for comparison purpose. The main peak at around 456 cm^{-1} is the symmetric stretching vibration mode (F_{2g}) of CeO_8 unit [38], and the peak at ~240 cm^{-1} is due to the second-order transverse acoustic mode (2TA) of CeO_2 [39]. The defect-induced mode (D) band starting from 520 to 670 cm^{-1} is related to the evolution of oxygen vacancies due to the presence of surface defects and/or different charge states of doping cations. And in some cases [40-42], the D band can be resolved into two peaks which are extrinsic (<600 cm^{-1}) and intrinsic oxygen vacancies (>600 cm^{-1}), respectively. According to the literature [43-44], the extrinsic oxygen vacancies mainly originate from the incorporation of bivalent or trivalent metal cations into CeO_2 matrix, while the intrinsic oxygen vacancies are attributed to the presence of Ce^{3+} ions (ionic radius for Ce^{3+}: 1.143 Å and for Ce^{4+}: 0.97 Å) in CeO_2 lattice. For comparison, the detailed Raman peak positions of the supported bimetallic catalysts and CeO_2NR support are listed in Table 2. With the introduction of MCo_2O_x (M=Fe, Ni and Cu) bimetallic oxides, the F_{2g} peaks all shift towards lower wavenumbers compared to the peak position of pure CeO_2NR support, which is indicative of the lattice distortion or formation of surface/interfacial solid solution. It is also noteworthy that the D band splits into two peaks for 10 wt% $FeCo_2O_x/CeO_2$NR and 10 wt% $CuCo_2O_x/CeO_2$NR catalysts, suggesting the generation of extrinsic oxygen vacancies due to the substitution of Ce^{4+} with the foreign Co/Fe/Cu ions. And for 10 wt% $NiCo_2O_x/CeO_2$NR, the peak splitting is negligible, implying that the intrinsic oxygen vacancy is the dominant type in contrast to the supported Fe-Co and Cu-Co bimetallic counterparts. For comparison, the Raman spectra of the 10% Co_3O_4/CeO_2NR catalyst and CeO_2NR support are shown in Fig. 1s, and it is clear that the addition of Co on CeO_2NR alters the 2TA and D bands coordination environment.

The relative surface concentration of Ce^{3+} can be estimated based on the XPS spectra of Ce 3d. As shown in Figure 2b, the spectra of Ce 3d are resolved into ten peaks, of which six peaks labeled as v (~881.6 eV), v'' (~888.2), v''' (~897.5 eV), u (~900.1 eV), u'' (~906.7 eV), and u''' (~916.0 eV) are assigned to Ce^{4+}, and for Ce^{3+} valence state, the peaks are denoted as v_0 (~879.6 eV), v' (~883.6

eV), *u₀* (~898.1 eV) and *u'* (~902.0 eV). By integrating each peak area, the relative amount of Ce^{3+} on the surface of the catalysts can be determined from the following equations:

$$[Ce^{3+}] = \frac{A_{v_0} + A_{v'} + A_{u_0} + A_{u'}}{A_{v_0} + A_{v'} + A_{u_0} + A_{u'} + A_{v} + A_{v''} + A_{v'''} + A_{u} + A_{u''} + A_{u'''}}$$

As can be seen in Figure 2 (b), 10 wt% $NiCo_2O_x/CeO_2NR$ shows the highest [Ce^{3+}] (14%) among three catalysts, which is in accord with the Raman result (Figure 2(a)). And after co-deposition of Co and M (M=Fe, Ni and Cu) onto CeO_2NR support, the surface/interfacial lattice defects configuration are greatly altered. The Raman results show that the extrinsic oxygen vacancies are introduced for 10 wt% $FeCo_2O_x/CeO_2NR$ and 10 wt% $CuCo_2O_x/CeO_2NR$ and the intrinsic oxygen vacancies are modified for 10 wt% $NiCo_2O_x/CeO_2NR$, and the XPS results further confirm these lattice structural changes by the variances of Ce^{3+} content, both of which indicate a strong metal(oxide)-support interaction at the interface.

The composition and oxidation state of the surface species were further investigated using XPS, and Figure 3 displays the spectra of Fe 2p, Ni 2p, Cu 2p and Co 2p from each bimetallic catalyst sample. For 10 wt% $FeCo_2O_x/CeO_2NR$, Fe 2p region displays the spin-orbit split doublet of Fe $2p_{1/2}$ and $2p_{3/2}$, and their separation ($\Delta = 2p_{1/2}–2p_{3/2}$) is 13.7 eV. The main peak Fe $2p_{3/2}$ can be deconvoluted into three subpeaks centered at 711.6 eV, 716.1 eV and 719.6 eV, which come from the contribution of Fe^{2+} species, Fe^{3+} species and a satellite feature [45-46]. However, it needs to be mentioned that both Fe $2p_{1/2}$ and $2p_{3/2}$ region shift to higher binding energies as compared to the corresponding peak positions reported in literatures [45, 47-48]. This chemical shift seems to be unclear at present, but it can be inferred possibly that the formation of Fe-O-Ce and Fe-O-Co bonds could contribute to the chemical coordination environment variation of Fe in the 10 wt% $FeCo_2O_x/CeO_2NR$ sample. The Ni 2p spectrum of the 10 wt% $NiCo_2O_x/CeO_2NR$ catalyst features the spin-orbital coupling Ni $2p_{1/2}$ and $2p_{3/2}$ at 872.1 eV and 854.5 eV, together with a shake-up satellite peak at 860.9 eV. According to the reference, those peaks are attributed to Ni^{2+} species [49]. Peak fitting analysis of the Cu 2p spectrum from the 10 wt% $CuCo_2O_x/CeO_2NR$ sample displays two intense peaks corresponding to Cu $2p_{1/2}$ (953.3 eV) and Cu $2p_{3/2}$ (933.5 eV), respectively. And both peaks are accompanied by a respective satellite peak centered at 941.6 eV and 961.4 eV. These two pairs of peaks confirm that the oxidization state of Cu is +2 in the 10 wt% $CuCo_2O_x/CeO_2NR$ catalyst [50]. The most interesting region is Co 2p of three supported MCo_2O_x (M=Fe, Ni and Cu) bimetallic catalysts. Comparatively, the Co $2p_{3/2}$ peak of supported Fe-Co and Ni-Co bimetallic catalysts samples can be deconvoluted into two major components, which are Co^{3+} at lower binding energy (~779.0 eV) and Co^{2+} at relatively higher binding energy (~780.3 eV), respectively. Meanwhile, the ratio of Co^{3+} to Co^{2+} species can be estimated based on the corresponding peak area, and it is noted that the Co^{3+}/Co^{2+} ratio for the 10 wt% $FeCo_2O_x/CeO_2NR$ catalyst (0.90) is much higher than that of the 10 wt% $NiCo_2O_x/CeO_2NR$ catalyst (0.35). Interestingly, the deconvolution of Co $2p_{3/2}$ peak for the 10 wt% $CuCo_2O_x/CeO_2NR$ catalyst indicates that the cobalt species are only in the +3 oxidized state (~779.6 eV). And the peak position of Co^{3+} $2p_{3/2}$ for the 10 wt% $CuCo_2O_x/CeO_2NR$ catalyst shifts slightly to higher value compared to those in the Fe-Co and Ni-Co bimetallic counterparts, indicating a stronger electronic interaction between Cu and Co cations. In literature, a general consensus is that the octahedrally coordinated Co^{3+} cations primarily serve as the active sites and are favorable for the catalytic oxidation of carbon monoxide, while tetrahedrally coordinated Co^{2+} are considered to be the inactive cations especially for the spinel structured Co_3O_4 [29, 51-52].

Based on the XPS analysis, both Fe^{2+} and Fe^{3+} for Fe, as well as Co^{3+} and Co^{2+} for Co coexist in the 10 wt% $FeCo_2O_x/CeO_2NR$ catalysts. As for the 10 wt% $NiCo_2O_x/CeO_2NR$ catalyst, the presence of Ni^{2+} of Ni, along with Co^{2+} and Co^{3+} of Co are confirmed. However, only Cu^{2+} and

Co^{3+} can be observed on the surface of the 10 wt% $CuCo_2O_x/CeO_2NR$ catalyst. Based on the findings above, it can be inferred that M^{2+} (M=Fe, Ni and Cu) substitutes the Co^{2+} in Co_3O_4 species (shown in Figure 3e). As Cu^{2+} cations replace all tetrahedrally coordinated Co^{2+} on the surface of supported $CuCo_2O_x$ bimetallic catalysts (no Co^{2+} is found on the surface of the sample shown in Figure 3d), the 10 wt% $CuCo_2O_x/CeO_2NR$ catalyst presents better catalytic performance (Figure 7a) in CO oxidation reaction owing to providing abundant active sites of both Cu^{2+} and Co^{3+} on the surface.

The particle size and morphology of CeO_2NR supported MCo_2O_x (M=Fe, Ni and Cu) catalysts were characterized by TEM and HAADF-STEM. Both TEM and STEM images in Figure 4 (a-c) and (g-i) clearly show the rod-like structure of CeO_2 support range from 5 to 10 nm in diameter and 50 to 100 nm in length. For the HRTEM images shown in Figure 4(d-f), it can be observed that CeO_2NR supported MCo_2O_x catalysts possess rough surfaces and significant amount of surface defects, consistent with the Raman results discussed above. The lattice fringes are measured about 0.31 nm, which is assigned to the (111) lattice plane exposed by CeO_2NR support. In addition, small clusters can be clearly found on the surface of CeO_2NR, as circled in Figure 4e and 4f, which are indicative of the bimetallic oxide species. To investigate the actual chemical composition of supported Co-M (M=Fe, Ni and Cu) catalysts, EDS analysis was performed and shown in Figure 4 (j-l). The EDS results confirm the atomic ratio of Co to Fe, Co to Ni and Co to Cu is close to 2:1 ratio (Co:Fe=0.21:0.11; Co:Ni=0.18: 0.09; Co:Cu=0.16: 0.09).

3.2 Reduction properties (H_2-TPR)

H_2-TPR was carried out to probe the reducibility (reduction temperature and hydrogen consumption) of the as-prepared nanocatalysts, and the profiles are shown in Figure 5. It is obvious that the reducibility of CeO_2NR supported MCo_2O_x (M=Fe, Ni and Cu) bimetallic catalysts varies considerably with different combinations of the second transition metal cation and cobalt. The H_2-TPR curve of 10 wt% $FeCo_2O_x/CeO_2NR$ catalyst exhibits mainly three reduction peaks at 201 °C, 330 °C, and 442 °C in the low temperature region (Figure 5a). Due to the variable valence states and non-stoichiometry of both iron (Fe^{2+} and Fe^{3+}) and cobalt (Co^{2+} and Co^{3+}) oxides, the assignment of the reduction peaks to specific Fe and Co species is challenging. Therefore, the TPR reduction peaks are assigned according to the previous report and our reference samples. Compared with the H_2-TPR results reported for Co-Fe mixed oxides with three main peaks at 350 °C, 460 °C, and 660 °C [53-54] and our H_2-TPR result for CeO_2NR supported monometallic Co_3O_4 (three main peaks at 228 °C, 284 °C, and 435 °C), the first small reduction peak located at 201 °C can be identified as the reduction of Co^{3+} to Co^{2+}, and the next broad peak at 330 °C is associated with overlapping features from the reduction of Co^{2+} to Co^0, Fe_2O_3 to Fe_3O_4 and Fe_3O_4 to Fe^0. The last reduction peak at 442 °C is attributed to the surface reduction of Ce^{4+} to Ce^{3+} for CeO_2NR support. It should be noted that the addition of CeO_2NR support clearly promotes the low temperature reducibility of Co-Fe bimetallic clusters from 350 °C, 460 °C, and 660 °C [53] to 201 °C, 330 °C, and 442 °C (Figure 5a), indicating a strong promoting effect of CeO_2NR and possible interfacial interactions between Co-Fe clusters and CeO_2NR. Meanwhile, the presence of Fe in the supported Fe-Co bimetallic catalyst also shows a promotion effect for the reduction of Co^{3+} to Co^{2+} in Co_3O_4 from 228 °C in CeO_2NR supported monometallic Co_3O_4 to 201 °C in CeO_2NR supported Fe-Co bimetallic catalyst.

For 10 wt% $NiCo_2O_x/CeO_2NR$ catalyst, there are also three reduction peaks at 204 °C, 274 °C, and 360 °C displayed in the H_2-TPR profile below 500 °C. Based on the results in the previous reports [55-56], the first reduction peak at 204 °C can be ascribed to the reduction of Co^{3+} to Co^{2+} (from $NiCo_2O_4$ to $NiCoO_2$), while the main reduction peak (the second reduction peak) at 274 °C corresponds to the reduction from Co^{2+} to Co^0. And the third reduction peak at 360 °C is associated with the reduction of Ni^{2+} to Ni^0 and Ce^{4+} to Ce^{3+} as reported previously [57-58]. Clearly the addition of Ni promotes the low temperature reducibility of cobalt oxides according to the reduction temperature from 228 °C and 284 °C in CeO_2NR supported monometallic Co_3O_4 to 204 °C and 274 °C (Figure 5a).

In the case of the 10 wt% $CuCo_2O_x/CeO_2$NR sample, the H_2-TPR profile shows three reduction peaks at 147 °C, 171 °C, and 207 °C as well below 300 °C. According to the literatures [55, 59-60], the first reduction peak at 147 °C can be attributed to the reduction of well-dispersed CuO small clusters. The main reduction peak centered at 171 °C corresponds to the reduction of Cu^{2+} to Cu^0 overlapping with the fractional reduction of Co^{3+} to Co^{2+} or the direct reduction of $CuCo_2O_x$, and the third reduction peak at 207 °C can be correlated to the reduction from of Co^{2+} to Co^0. By comparison, the 10 wt% $CuCo_2O_4/CeO_2$NR catalyst exhibits superior low-temperature reducibility, with the lowest reduction temperature among three supported bimetallic catalysts.

In addition, the reducibility of the as-discussed bimetallic catalysts was further evaluated by quantifying the H_2 consumptions as depicted in Figure 5b and the results are shown in Table 3 as well. The H_2 consumption due to the surface reduction (from 30 to 300 °C) is ranked as follows: 10 wt% $CuCo_2O_x/CeO_2$NR>10 wt% $NiCo_2O_x/CeO_2$NR>10 wt% $FeCo_2O_x/CeO_2$NR. Collectively, the 10 wt% $CuCo_2O_4/CeO_2$NR catalyst is found to be the most reducible in terms of reduction temperature and hydrogen consumption among three bimetallic samples at low-temperature region (<300 °C).

3.3 Oxygen storage capacity (OSC) and activated oxygen species

O_2 pulse chemisorption analysis was used to determine the dynamic oxygen adsorption behavior and oxygen storage capacity, and the profiles of CeO_2NR supported MCo_2O_x (M=Fe, Ni and Cu) catalysts are shown in Figure 6a. Table 1 also provides the detailed OSC values for these samples. All CeO_2NR supported samples possess very high oxygen storage capacity compared to the reported values [4, 61], revealing the unique surface structures of CeO_2NR support that can adsorb and store the reactive oxygen. For the supported MCo_2O_x (M=Fe, Ni and Cu) samples, the OSC values are varied in the order of 10 wt% $CuCo_2O_x/CeO_2$NR (641.0 μmol g^{-1})>10 wt% $FeCo_2O_x/CeO_2$NR (468.2 μmol g^{-1})>10 wt% $NiCo_2O_x/CeO_2$NR (423.6 μmol g^{-1}).

Furthermore, O_2-TPD was carried out to investigate the reactivity and mobility of different oxygen species that involved in oxidation reactions, and the spectra of the above-mentioned catalysts are shown in Figure 6b. Normally, there are three types of oxygen [62-63]: the physically adsorbed oxygen O_2 (blue shadow), chemically adsorbed oxygen O_2^-/O^- (red shadow) and the bulk lattice oxygen (green shadow). As can be seen, the synergism between cobalt with the second transition metal (Fe, Ni and Cu) plays an important role in modulating the oxygen mobility. And comparably, CeO_2NR supported $NiCo_2O_x$ sample has more active surface oxygen than supported $FeCo_2O_x$ and $CuCo_2O_x$ counterparts, appeared as the larger peak area of the first two desorption peaks (A_1 and A_2). Nevertheless, 10 wt% $CuCo_2O_x/CeO_2$NR has the highest concentration of activated lattice oxygen (A_3).

3.4 Catalytic behavior

The catalytic activity of CeO_2NR supported bimetallic MCo_2O_x (M=Fe, Ni and Cu) catalysts over CO oxidation reaction is shown in Figure 7a, and the CO catalytic performance of CeO_2NR supported monometallic Co_3O_4 is also included for comparison purpose. The order of CO oxidation activity can be clearly ranked as: 10 wt% $CuCo_2O_x/CeO_2$NR (T_{50}= 95 °C and T_{90}= 148 °C) > 10 wt% Co_3O_4/CeO_2NR (T_{50}= 101 °C and T_{90}= 156 °C) > 10 wt% $FeCo_2O_x/CeO_2$NR (T_{50}= 129 °C and T_{90}= 193 °C) > 10 wt% $NiCo_2O_x/CeO_2$NR (T_{50}= 147 °C and T_{90}= 196 °C). Mars-van Krevelen mechanism has been widely adopted for explaining CO oxidation over CeO_2 supported transition metal oxide catalysts which involves the reaction between chemisorbed CO with surface lattice O species of CeO_2NR support, thus forming the oxygen vacancies. Then, the replenishment of the as-formed oxygen vacancies by gas-phase oxygen or a "lattice-oxygen" migration process will occur during the reaction. A schematic drawing of possible reaction mechanism is proposed as shown in Figure 8, in which the supported bimetallic oxides MCo_2O_x (M=Fe, Ni and Cu) serve as the primary adsorption sites for CO molecules, then the adsorbed CO species react with the mobile surface oxygen of CeO_2NR support, meanwhile leaving the oxygen vacancies that sequentially act as the adsorption sites to trap gas-phase oxygen molecules or trigger the transport of mobile bulk oxygen. The temperature-programmed desorption of CO (CO-TPD) measurements were also conducted to examine the CO adsorption and desorption behavior of the prepared catalysts. From Figure S2, it is noted that the second transition metals (Fe, Ni Cu) altered the CO adsorption property of CeO_2NR supported MCo_2O_x bimetallic catalysts. The 10 wt% $CuCo_2O_x/CeO_2$NR catalyst exhibited the strongest desorption peaks, while the CO-TPD profiles of 10 wt% $NiCo_2O_x/CeO_2$NR is similar to that of the monometallic 10 wt% Co_3O_4/CeO_2NR. The 10 wt% $FeCo_2O_x/CeO_2$NR catalyst showed the weakest intensity of gas desorption. These CO-TPD results provide evidence for more absorbed CO over CeO_2NR supported Co-Cu bimetallic oxides, which further reveals the origin of superior CO oxidation performance for the Co-Cu catalyst. In our case, the catalytic behavior toward CO oxidation are well correlated with the OSC and oxygen mobility. The 10 wt% $CuCo_2O_x/CeO_2$NR catalyst with the highest OSCC (641.0 μmol O_2 g_{cat}^{-1}) and the bulk lattice oxygen mobility (A_3=0.81 in TPD) exhibits superior low-temperature CO conversion performance, followed by 10 wt% $FeCo_2O_x/CeO_2$NR catalyst (OSCC: 468.2 μmol O_2 g_{cat}^{-1} and A_3 in TPD: 0.63) and 10 wt% $NiCo_2O_x/CeO_2$NR catalyst (OSCC: 423.6 μmol O_2 g_{cat}^{-1} and A_3 in TPD:

0.54).

The performance of the catalysts in terms of C_3H_8 conversion were further evaluated as a function of temperature between 100 °C and 600 °C, and the light-off curves are show in Figure 7b. The T_{50} values of the as-discussed bimetallic MCo_2O_x (M=Fe, Ni and Cu) catalysts are similar, with 320 °C, 322 °C and 338 °C for 10 wt% $FeCo_2O_x/CeO_2NR$, 10 wt% $NiCo_2O_x/CeO_2NR$ and 10 wt% $CuCo_2O_x/CeO_2NR$ catalysts, but relatively higher than the monometallic 10 wt% Co_3O_4/CeO_2NR catalyst (T_{50}= 302 °C). However, the maximum conversion rate for C_3H_8 oxidation on the catalysts follow the sequence of 10 wt% $NiCo_2O_x/CeO_2NR$ (88.2%)>10 wt% $FeCo_2O_x/CeO_2NR$ (79.8%)>10 wt% $CuCo_2O_x/CeO_2NR$ (79.1%)>10 wt% Co_3O_4/CeO_2NR (67.6%). It was worth noting that the observed catalytic activity toward the C_3H_8 conversion limit is closely related to the concentration of Ce^{3+} species, as well as the physically adsorbed molecular oxygen O_2 (A_1 in TPD) and chemically adsorbed oxygen O_2^-/O^- species (A_2 in TPD). It is well known in the literature that the "activated" or "reactive" oxygen species (O^{2-}, O_2^-, O_2^{2-} and O^-) are crucial for hydrocarbon deep oxidation [64-66]. In this case, the 10 wt% $NiCo_2O_x/CeO_2NR$ bimetallic catalyst with the highest concentration of Ce^{3+} (Ce^{3+}/Ce_{total} = 14.0% from XPS) and the physically/chemically adsorbed O_2 species ($A_1 + A_2 = 1.93$ in O_2-TPD), exhibits the best C_3H_8 oxidation performance.

It is well known that the catalytic CO oxidation over reducible oxide supported transition metal catalysts is dependent on the CO adsorption over metal catalyst and bulk lattice oxygen mobility of oxide support [67]. While total catalytic oxidation of propane involves dissociated adsorption of C_3H_8 and then reaction with the surface-active oxygen of oxide support [68]. Due to the disparate overall heat of reaction (-283 kJ/mol for CO oxidation vs. -2044 kJ/mol for C_3H_8 oxidation) [69], bond dissociation energy (358 kJ/mol for C-O bond vs. 413 kJ/mol for C-H bond) [70], and adsorption energy of the reactants over different catalysts surfaces, these catalysts exhibited dissimilar catalytic behavior between CO oxidation and C_3H_8 oxidation.

4. CONCLUSION

In summary, we investigated the synergistic effect between Co and the second transition metal cation M (M=Fe, Ni and Cu) in CeO_2NR supported Co-M bimetallic oxides catalysts, along with the interaction between the bimetallic MCo_2O_x species and CeO_2NR support. Based upon the morphology and structural characterization, the incorporation of the second transition metal (Fe, Ni and Cu) did not affect the crystallite size. However, the synergism between cobalt and the second transition metal cation M leads to the obvious differences in the chemical state of surface-active species, thus altering the reducibility, lattice oxygen mobility and catalytic activity over CO and C_3H_8 oxidation. It was found out that CeO_2NR supported Co-Cu bimetallic oxides showed the best performance with the remarkable low-temperature reducibility and CO oxidation activity among three bimetallic MCo_2O_x (M=Fe, Ni and Cu) catalysts. The CO conversion performance are well correlated to the oxygen storage capacity and the bulk lattice oxygen mobility of the catalysts. As for the oxidation of C_3H_8, 10 wt% $NiCo_2O_x/CeO_2$NR exhibited the best performance, especially above 330 °C. The catalytic activity toward C_3H_8 oxidation can be closely related to the concentration of Ce^{3+} species, and the concentration of physically/chemically adsorbed oxygen species. The strong metal(oxides)-support interaction was also confirmed, which represents as the shrinkage of the lattice constant of CeO_2NR support and the formation of the extrinsic oxygen vacancies or the modulation of the intrinsic oxygen vacancies.

ACKNOWLEDGEMENTS

The financial support was provided by the National Science Foundation (CBET-1856729 and CHE-1657943) and the American Chemical Society Petroleum Research Fund (#52323). This project also receives partial financial support from Alabama Water Institute and Alabama Transportation Institute. The use of TEM facilities at Central Analytical Facility (CAF) of the University of Alabama is gratefully acknowledged. The authors also thank Yu Cheng (University of Virginia) for the graphic design.

REFERENCES

1. Wang, R.; Crozier, P. A.; Sharma, R., Structural transformation in ceria nanoparticles during redox processes. *J. Phys. Chem. C* **2009,** *113* (14), 5700-5704.
2. Wang, R.; Crozier, P. A.; Sharma, R.; Adams, J. B., Measuring the redox activity of individual catalytic nanoparticles in cerium-based oxides. *Nano Lett.* **2008,** *8* (3), 962-967.
3. Liu, X.; Zhou, K.; Wang, L.; Wang, B.; Li, Y., Oxygen vacancy clusters promoting reducibility and activity of ceria nanorods. *J. Am. Chem. Soc.* **2009,** *131* (9), 3140-3141.
4. Mai, H.-X.; Sun, L.-D.; Zhang, Y.-W.; Si, R.; Feng, W.; Zhang, H.-P.; Liu, H.-C.; Yan, C.-H., Shape-selective synthesis and oxygen storage behavior of ceria nanopolyhedra, nanorods, and nanocubes. *J. Phys. Chem. B* **2005,** *109* (51), 24380-24385.
5. Campbell, C. T.; Peden, C. H., Oxygen vacancies and catalysis on ceria surfaces. *Science* **2005,** *309* (5735), 713-714.
6. Xu, J.; Harmer, J.; Li, G.; Chapman, T.; Collier, P.; Longworth, S.; Tsang, S. C., Size dependent oxygen buffering capacity of ceria nanocrystals. *Chem. Commun.* **2010,** *46* (11), 1887-1889.
7. Trovarelli, A., Catalytic properties of ceria and CeO_2-containing materials. *Catal. Rev.-Sci. Eng.* **1996,** *38* (4), 439-520.
8. Mamontov, E.; Egami, T.; Brezny, R.; Koranne, M.; Tyagi, S., Lattice defects and oxygen storage capacity of nanocrystalline ceria and ceria-zirconia. *J. Phys. Chem. B* **2000,** *104* (47), 11110-11116.
9. López, J. M.; Gilbank, A. L.; García, T.; Solsona, B.; Agouram, S.; Torrente-Murciano, L., The prevalence of surface oxygen vacancies over the mobility of bulk oxygen in nanostructured ceria for the total toluene oxidation. *Appl. Catal., B* **2015,** *174*, 403-412.
10. Zhang, S.; Huang, Z.-Q.; Ma, Y.; Gao, W.; Li, J.; Cao, F.; Li, L.; Chang, C.-R.; Qu, Y., Solid frustrated-Lewis-pair catalysts constructed by regulations on surface defects of porous nanorods of CeO_2. *Nat. Commun.* **2017,** *8*, 15266.
11. Kopelent, R.; van Bokhoven, J. A.; Szlachetko, J.; Edebeli, J.; Paun, C.; Nachtegaal, M.; Safonova, O. V., Catalytically active and spectator Ce3+ in ceria-supported metal catalysts. *Angew. Chem. Int. Ed* **2015,** *54* (30), 8728-8731.
12. Si, R.; Flytzani-Stephanopoulos, M., Shape and crystal-plane effects of nanoscale ceria on the activity of Au-CeO_2 catalysts for the water–gas shift reaction. *Angew. Chem. Int. Ed* **2008,** *47* (15), 2884-2887.
13. Jones, J.; Xiong, H.; DeLaRiva, A. T.; Peterson, E. J.; Pham, H.; Challa, S. R.; Qi, G.; Oh, S.; Wiebenga, M. H.; Hernández, X. I. P., Thermally stable single-atom platinum-on-ceria catalysts via atom trapping. *Science* **2016,** *353* (6295), 150-154.
14. Agarwal, S.; Lefferts, L.; Mojet, B. L.; Ligthart, D. M.; Hensen, E. J.; Mitchell, D. R.; Erasmus, W. J.; Anderson, B. G.; Olivier, E. J.; Neethling, J. H., Exposed surfaces on shape-controlled ceria nanoparticles revealed through AC-TEM and water–gas shift reactivity. *ChemSusChem* **2013,** *6* (10), 1898-1906.
15. Mock, S. A.; Sharp, S. E.; Stoner, T. R.; Radetic, M. J.; Zell, E. T.; Wang, R., CeO_2 nanorods-supported transition metal catalysts for CO oxidation. *J. Colloid Interface Sci.* **2016,** *466*, 261-267.
16. Wang, Y.; Chen, Z.; Han, P.; Du, Y.; Gu, Z.; Xu, X.; Zheng, G., Single-atomic Cu with multiple oxygen vacancies on ceria for electrocatalytic CO_2 reduction to CH_4. *ACS Catal.* **2018,** *8* (8), 7113-7119.
17. Ta, N.; Liu, J.; Chenna, S.; Crozier, P. A.; Li, Y.; Chen, A.; Shen, W., Stabilized gold nanoparticles on ceria nanorods by strong interfacial anchoring. *J. Am. Chem. Soc.* **2012,** *134* (51), 20585-20588.

18. Huang, X.-S.; Sun, H.; Wang, L.-C.; Liu, Y.-M.; Fan, K.-N.; Cao, Y., Morphology effects of nanoscale ceria on the activity of Au/CeO_2 catalysts for low-temperature CO oxidation. *Appl. Catal., B* **2009,** *90* (1-2), 224-232.
19. Lin, Y.; Wu, Z.; Wen, J.; Ding, K.; Yang, X.; Poeppelmeier, K. R.; Marks, L. D., Adhesion and atomic structures of gold on ceria nanostructures: the role of surface structure and oxidation state of ceria supports. *Nano Lett.* **2015,** *15* (8), 5375-5381.
20. Cui, Y.; Dai, W.-L., Support morphology and crystal plane effect of Cu/CeO_2 nanomaterial on the physicochemical and catalytic properties for carbonate hydrogenation. *Catal. Sci. Technol.* **2016,** *6* (21), 7752-7762.
21. Li, J.; Lu, G.; Wu, G.; Mao, D.; Wang, Y.; Guo, Y., Promotional role of ceria on cobaltosic oxide catalyst for low-temperature CO oxidation. *Catal. Sci. Technol.* **2012,** *2* (9), 1865-1871.
22. Ma, Z., Cobalt oxide catalysts for environmental remediation. *Curr. Catal.* **2014,** *3* (1), 15-26.
23. Zhou, Y.; Li, Y.; Shen, W., Shape engineering of oxide nanoparticles for heterogeneous catalysis. *Chem. – Asian J.* **2016,** *11* (10), 1470-1488.
24. Xie, X.; Li, Y.; Liu, Z.-Q.; Haruta, M.; Shen, W., Low-temperature oxidation of CO catalysed by Co_3O_4 nanorods. *Nature* **2009,** *458* (7239), 746.
25. Li, Y.; Hasin, P.; Wu, Y., $Ni_xCo_{3-x}O_4$ nanowire arrays for electrocatalytic oxygen evolution. *Adv. Mater.* **2010,** *22* (17), 1926-1929.
26. Ramasamy, K. K.; Gray, M.; Job, H.; Wang, Y., Direct syngas hydrogenation over a Co–Ni bimetallic catalyst: Process parameter optimization. *Chem. Eng. Sci.* **2015,** *135*, 266-273.
27. Chen, Y.; Zhang, Q.; Zhang, Z.; Zhou, X.; Zhong, Y.; Yang, M.; Xie, Z.; Wei, J.; Zhou, Z., Two better than one: cobalt–copper bimetallic yolk–shell nanoparticles supported on graphene as excellent cathode catalysts for Li–O_2 batteries. *J. Mater. Chem. A* **2015,** *3* (34), 17874-17879.
28. Ma, L.; Seo, C. Y.; Chen, X.; Sun, K.; Schwank, J. W., Indium-doped Co_3O_4 nanorods for catalytic oxidation of CO and C_3H_6 towards diesel exhaust. *Appl. Catal., B* **2018,** *222*, 44-58.
29. Zhou, M.; Cai, L.; Bajdich, M.; García-Melchor, M.; Li, H.; He, J.; Wilcox, J.; Wu, W.; Vojvodic, A.; Zheng, X., Enhancing Catalytic CO Oxidation over Co_3O_4 Nanowires by Substituting Co2+ with Cu2+. *ACS Catal.* **2015,** *5* (8), 4485-4491.
30. Ren, Z.; Botu, V.; Wang, S.; Meng, Y.; Song, W.; Guo, Y.; Ramprasad, R.; Suib, S. L.; Gao, P.-X., Monolithically Integrated Spinel $M_xCo_{3-x}O_4$ (M=Co, Ni, Zn) Nanoarray Catalysts: Scalable Synthesis and Cation Manipulation for Tunable Low-Temperature CH_4 and CO Oxidation. *Angew. Chem. Int. Ed* **2014,** *53* (28), 7223-7227.
31. Binder, A. J.; Toops, T. J.; Unocic, R. R.; Parks II, J. E.; Dai, S., Low-Temperature CO Oxidation over a Ternary Oxide Catalyst with High Resistance to Hydrocarbon Inhibition. *Angew. Chem. Int. Ed* **2015,** *54* (45), 13263-13267.
32. Wang, R.; Dangerfield, R., Seed-mediated synthesis of shape-controlled CeO_2 nanocrystals. *RSC Adv.* **2014,** *4* (7), 3615-3620.
33. Hossain, S. T.; Azeeva, E.; Zhang, K.; Zell, E. T.; Bernard, D. T.; Balaz, S.; Wang, R., A comparative study of CO oxidation over Cu-O-Ce solid solutions and CuO/CeO_2 nanorods catalysts. *Appl. Surf. Sci.* **2018,** *455*, 132-143.
34. Lovón, A. S. P.; Lovón-Quintana, J. J.; Almerindo, G. I.; Valença, G. P.; Bernardi, M. I. B.; Araújo, V. D.; Rodrigues, T. S.; Robles-Dutenhefner, P. A.; Fajardo, H. V., Preparation, structural characterization and catalytic properties of Co/CeO_2 catalysts for the steam reforming of ethanol and hydrogen production. *J. Power Sources* **2012,** *216*, 281-289.
35. Wang, R.; Wei, J.; Wei, H.; Yang, Y., Crystal plane dependent dopant migration that boosts catalytic oxidation. *Catal. Sci. Technol.* **2018,** *8* (23), 6084-6090.

36. Mahammadunnisa, S.; Manoj Kumar Reddy, P.; Lingaiah, N.; Subrahmanyam, C., NiO/$Ce_{1-x}Ni_xO_{2-\delta}$ as an alternative to noble metal catalysts for CO oxidation. *Catal. Sci. Technol.* **2013,** *3* (3), 730-736.
37. Li, Y.; Zhang, B.; Tang, X.; Xu, Y.; Shen, W., Hydrogen production from methane decomposition over Ni/CeO_2 catalysts. *Catal. Commun.* **2006,** *7* (6), 380-386.
38. Choudhury, B.; Chetri, P.; Choudhury, A., Oxygen defects and formation of Ce3+ affecting the photocatalytic performance of CeO_2 nanoparticles. *RSC Adv.* **2014,** *4* (9), 4663-4671.
39. Schilling, C.; Hofmann, A.; Hess, C.; Ganduglia-Pirovano, M. V., Raman Spectra of Polycrystalline CeO_2: A Density Functional Theory Study. *J. Phys. Chem. C* **2017,** *121* (38), 20834-20849.
40. Tan, J.; Lee, D.; Ahn, J.; Kim, B.; Kim, J.; Moon, J., Thermally driven in situ exsolution of Ni nanoparticles from (Ni, Gd) CeO_2 for high-performance solid oxide fuel cells. *J. Mater. Chem. A* **2018,** *6* (37), 18133-18142.
41. Acharya, S.; Gaikwad, V.; Sathe, V.; Kulkarni, S., Influence of gadolinium doping on the structure and defects of ceria under fuel cell operating temperature. *Appl. Phys. Lett.* **2014,** *104* (11), 113508.
42. Tseng, E. N.; Hsiao, Y.-T.; Chen, Y.-C.; Chen, S.-Y.; Gloter, A.; Song, J.-M., Magnetism and plasmonic performance of mesoscopic hollow ceria spheres decorated with silver nanoparticles. *Nanoscale* **2019**.
43. Guo, M.; Lu, J.; Wu, Y.; Wang, Y.; Luo, M., UV and Visible Raman Studies of Oxygen Vacancies in Rare-Earth-Doped Ceria. *Langmuir* **2011,** *27* (7), 3872-3877.
44. Bernardi, M. I. B.; Mesquita, A.; Béron, F.; Pirota, K. R.; de Zevallos, A. O.; Doriguetto, A. C.; de Carvalho, H. B., The role of oxygen vacancies and their location in the magnetic properties of $Ce_{1-x}Cu_xO_{2-\delta}$ nanorods. *Phys. Chem. Chem. Phys.* **2015,** *17* (5), 3072-3080.
45. Yamashita, T.; Hayes, P., Analysis of XPS spectra of Fe2+ and Fe3+ ions in oxide materials. *Appl. Surf. Sci.* **2008,** *254* (8), 2441-2449.
46. Zhou, T.; Cao, Z.; Zhang, P.; Ma, H.; Gao, Z.; Wang, H.; Lu, Y.; He, J.; Zhao, Y., Transition metal ions regulated oxygen evolution reaction performance of Ni-based hydroxides hierarchical nanoarrays. *Sci. Rep.* **2017,** *7*, 46154.
47. Uhlig, I.; Szargan, R.; Nesbitt, H. W.; Laajalehto, K., Surface states and reactivity of pyrite and marcasite. *Appl. Surf. Sci.* **2001,** *179* (1), 222-229.
48. Biesinger, M. C.; Payne, B. P.; Grosvenor, A. P.; Lau, L. W. M.; Gerson, A. R.; Smart, R. S. C., Resolving surface chemical states in XPS analysis of first row transition metals, oxides and hydroxides: Cr, Mn, Fe, Co and Ni. *Appl. Surf. Sci.* **2011,** *257* (7), 2717-2730.
49. Zou, W.; Ge, C.; Lu, M.; Wu, S.; Wang, Y.; Sun, J.; Pu, Y.; Tang, C.; Gao, F.; Dong, L., Engineering the NiO/CeO2 interface to enhance the catalytic performance for CO oxidation. *RSC Adv.* **2015,** *5* (119), 98335-98343.
50. Wang, X.; Liu, Y.; Peng, X.; Lin, B.; Cao, Y.; Jiang, L., Sacrificial Adsorbate Strategy Achieved Strong Metal–Support Interaction of Stable Cu Nanocatalysts. *ACS Appl. Energy Mater.* **2018,** *1* (4), 1408-1414.
51. Gu, D.; Jia, C.-J.; Weidenthaler, C.; Bongard, H.-J.; Spliethoff, B.; Schmidt, W.; Schüth, F., Highly Ordered Mesoporous Cobalt-Containing Oxides: Structure, Catalytic Properties, and Active Sites in Oxidation of Carbon Monoxide. *J. Am. Chem. Soc.* **2015,** *137* (35), 11407-11418.
52. Li, Y.; Shen, W., Morphology-dependent nanocatalysts: Rod-shaped oxides. *Chem. Soc. Rev.* **2014,** *43* (5), 1543-1574.

53. Abdelkader, A.; Daly, H.; Saih, Y.; Morgan, K.; Mohamed, M. A.; Halawy, S. A.; Hardacre, C., Steam reforming of ethanol over Co_3O_4–Fe_2O_3 mixed oxides. *Int. J. Hydrogen Energy* **2013,** *38* (20), 8263-8275.
54. Ali, S.; Mohd Zabidi, N. A.; Subbarao, D., Correlation between Fischer-Tropsch catalytic activity and composition of catalysts. *Chem. Centr. J.* **2011,** *5* (1), 68.
55. Zhang, S.; Zhu, X.; Zheng, C.; Hu, D.; Zhang, J.; Gao, X., Study on catalytic soot oxidation over spinel type ACo_2O_4 (A= Co, Ni, Cu, Zn) catalysts. *Aerosol Air Qual. Res.* **2017,** *17* (9), 2317-2327.
56. Lim, T. H.; Cho, S. J.; Yang, H. S.; Engelhard, M. H.; Kim, D. H., Effect of Co/Ni ratios in cobalt nickel mixed oxide catalysts on methane combustion. *Appl. Catal., A* **2015,** *505*, 62-69.
57. Xu, X.; Li, L.; Yu, F.; Peng, H.; Fang, X.; Wang, X., Mesoporous high surface area NiO synthesized with soft templates: Remarkable for catalytic CH_4 deep oxidation. *Mol. Catal.* **2017,** *441*, 81-91.
58. Tang, C.; Sun, B.; Sun, J.; Hong, X.; Deng, Y.; Gao, F.; Dong, L., Solid state preparation of NiO-CeO_2 catalyst for NO reduction. *Catal. Today* **2017,** *281*, 575-582.
59. Fierro, G.; Lo Jacono, M.; Inversi, M.; Dragone, R.; Porta, P., TPR and XPS study of cobalt–copper mixed oxide catalysts: evidence of a strong Co–Cu interaction. *Top. Catal.* **2000,** *10* (1), 39-48.
60. Mock, S. A.; Zell, E. T.; Hossain, S. T.; Wang, R., Effect of Reduction Treatment on CO Oxidation with CeO2 Nanorod-Supported CuOx Catalysts. *ChemCatChem* **2018,** *10* (1), 311-319.
61. Martínez-Arias, A.; Fernández-García, M.; Gálvez, O.; Coronado, J. M.; Anderson, J. A.; Conesa, J. C.; Soria, J.; Munuera, G., Comparative Study on Redox Properties and Catalytic Behavior for CO Oxidation of CuO/CeO_2 and CuO/$ZrCeO_4$ Catalysts. *J. Catal.* **2000,** *195* (1), 207-216.
62. Chen, Y.; Liu, D.; Yang, L.; Meng, M.; Zhang, J.; Zheng, L.; Chu, S.; Hu, T., Ternary composite oxide catalysts CuO/Co_3O_4–CeO_2 with wide temperature-window for the preferential oxidation of CO in H_2-rich stream. *Chem. Eng. J.* **2013,** *234*, 88-98.
63. Manto, M. J.; Xie, P.; Wang, C., Catalytic Dephosphorylation Using Ceria Nanocrystals. *ACS Catal.* **2017,** *7* (3), 1931-1938.
64. Zhang, P.; Lu, H.; Zhou, Y.; Zhang, L.; Wu, Z.; Yang, S.; Shi, H.; Zhu, Q.; Chen, Y.; Dai, S., Mesoporous MnCeOx solid solutions for low temperature and selective oxidation of hydrocarbons. *Nat. Commun.* **2015,** *6*, 8446.
65. Zasada, F.; Janas, J.; Piskorz, W.; Gorczyńska, M.; Sojka, Z., Total Oxidation of Lean Methane over Cobalt Spinel Nanocubes Controlled by the Self-Adjusted Redox State of the Catalyst: Experimental and Theoretical Account for Interplay between the Langmuir–Hinshelwood and Mars–Van Krevelen Mechanisms. *ACS Catal.* **2017,** *7* (4), 2853-2867.
66. Zhang, X.; You, R.; Li, D.; Cao, T.; Huang, W., Reaction Sensitivity of Ceria Morphology Effect on Ni/CeO_2 Catalysis in Propane Oxidation Reactions. *ACS Appl. Mater. Interfaces* **2017,** *9* (41), 35897-35907.
67. Liotta, L. F.; Wu, H.; Pantaleo, G.; Venezia, A. M., Co_3O_4 nanocrystals and Co_3O_4–MO_x binary oxides for CO, CH_4 and VOC oxidation at low temperatures: a review. *Catal. Sci. Technol.* **2013,** *3*(12), 3085-3102.
68. Tang, W.; Xiao, W.; Wang, S.; Ren, Z.; Ding, J.; Gao, P.-X., Boosting catalytic propane oxidation over PGM-free Co_3O_4 nanocrystal aggregates through chemical leaching: A comparative study with Pt and Pd based catalysts. *Appl. Catal., B* **2018,** *226*, 585-595.

69. Peck, R.; Becker, C. Experimental investigations and dynamic simulation of diesel particulate filter systems. *Chem. Eng. Technol.* **2009,** *32*(9), 1411-1422.

70. Xing, W.; Li, H.; Huang, G.; Cai, L. H.; Wu, J. Graphene oxide induced crosslinking and reinforcement of elastomers. *Compos. Sci. Technol.* **2017,** *144*, 223-229.

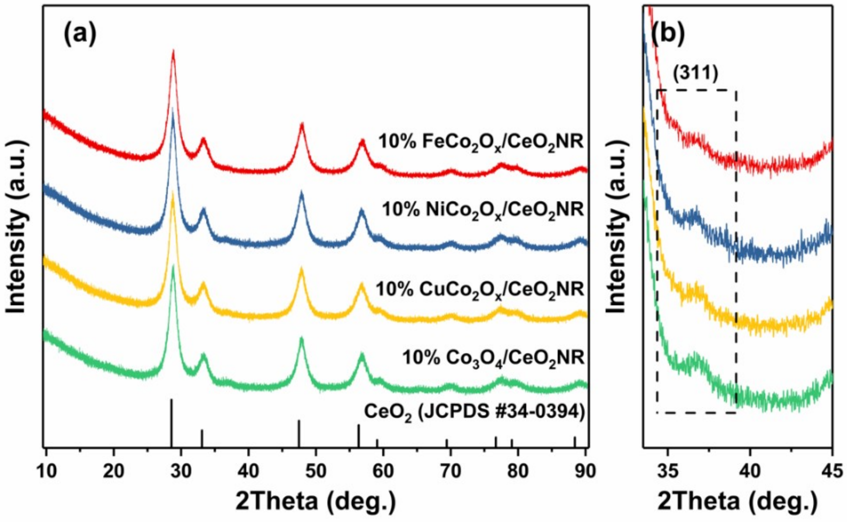

Figure 1. (a) XRD patterns and (b) an enlarged region of CeO_2NR supported Co_3O_4 and MCo_2O_x (M=Fe, Ni and Cu) catalysts.

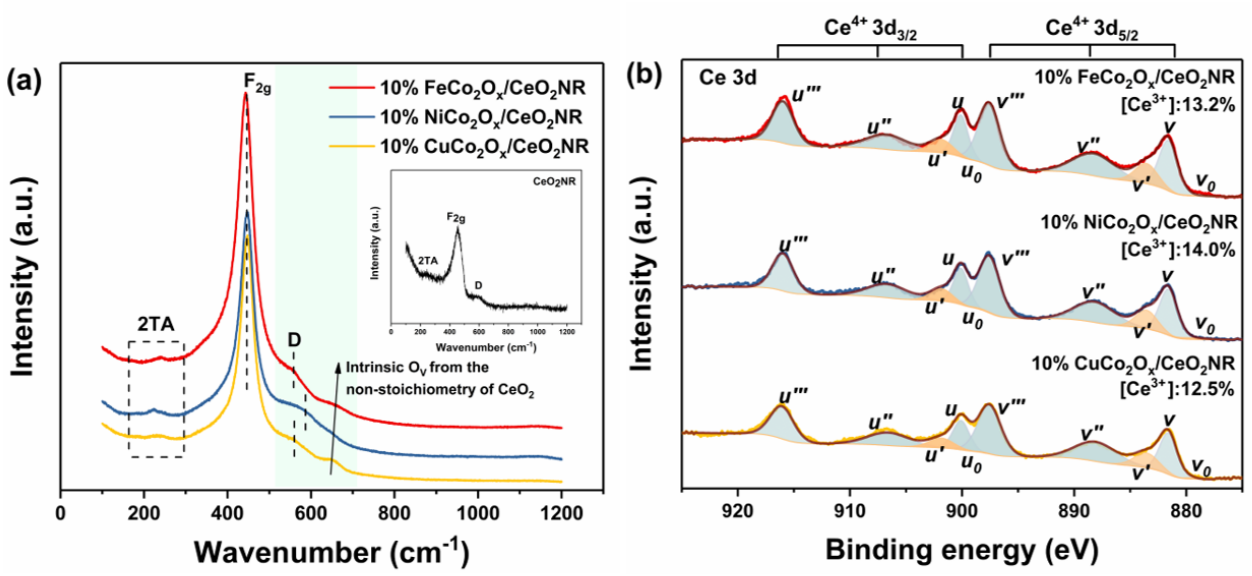

Figure 2. (a) Raman spectra of CeO$_2$NR supported MCo$_2$O$_x$ (M=Fe, Ni and Cu) catalysts and pure CeO$_2$NR support (inset), (b) XPS spectra of Ce 3d for CeO$_2$NR supported MCo$_2$O$_x$ (M=Fe, Ni and Cu) catalysts.

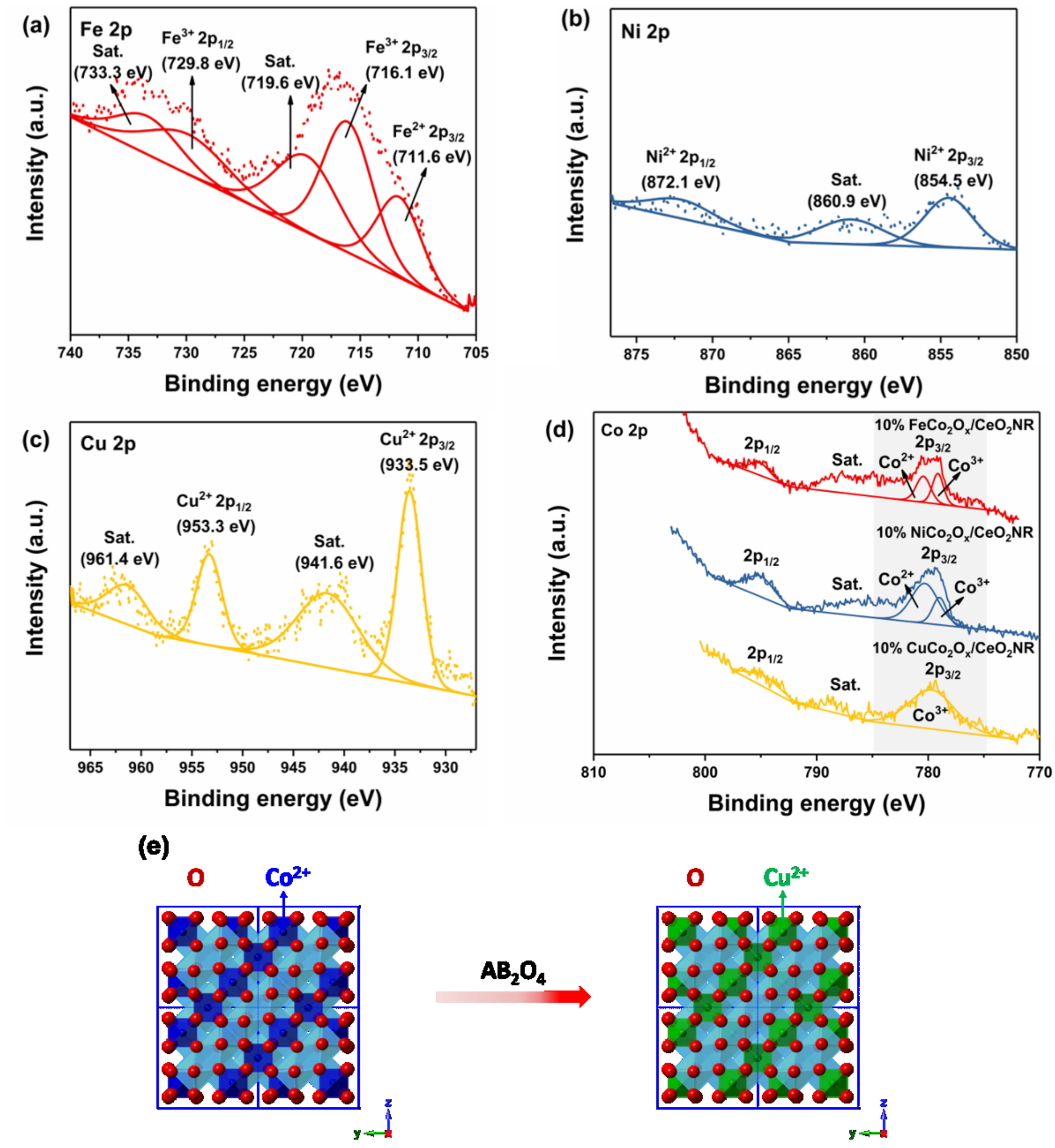

Figure 3. XPS spectra of (a) Fe 2p, (b) Ni 2p, (c) Cu 2p, (d) Co 2p for CeO_2NR supported MCo_2O_x (M=Fe, Ni and Cu) catalysts and (e) crystal structure of Co_3O_4 and $CuCo_2O_4$. (All curve fitting were performed based on a linear background, and "Sat." denotes the satellite peak).

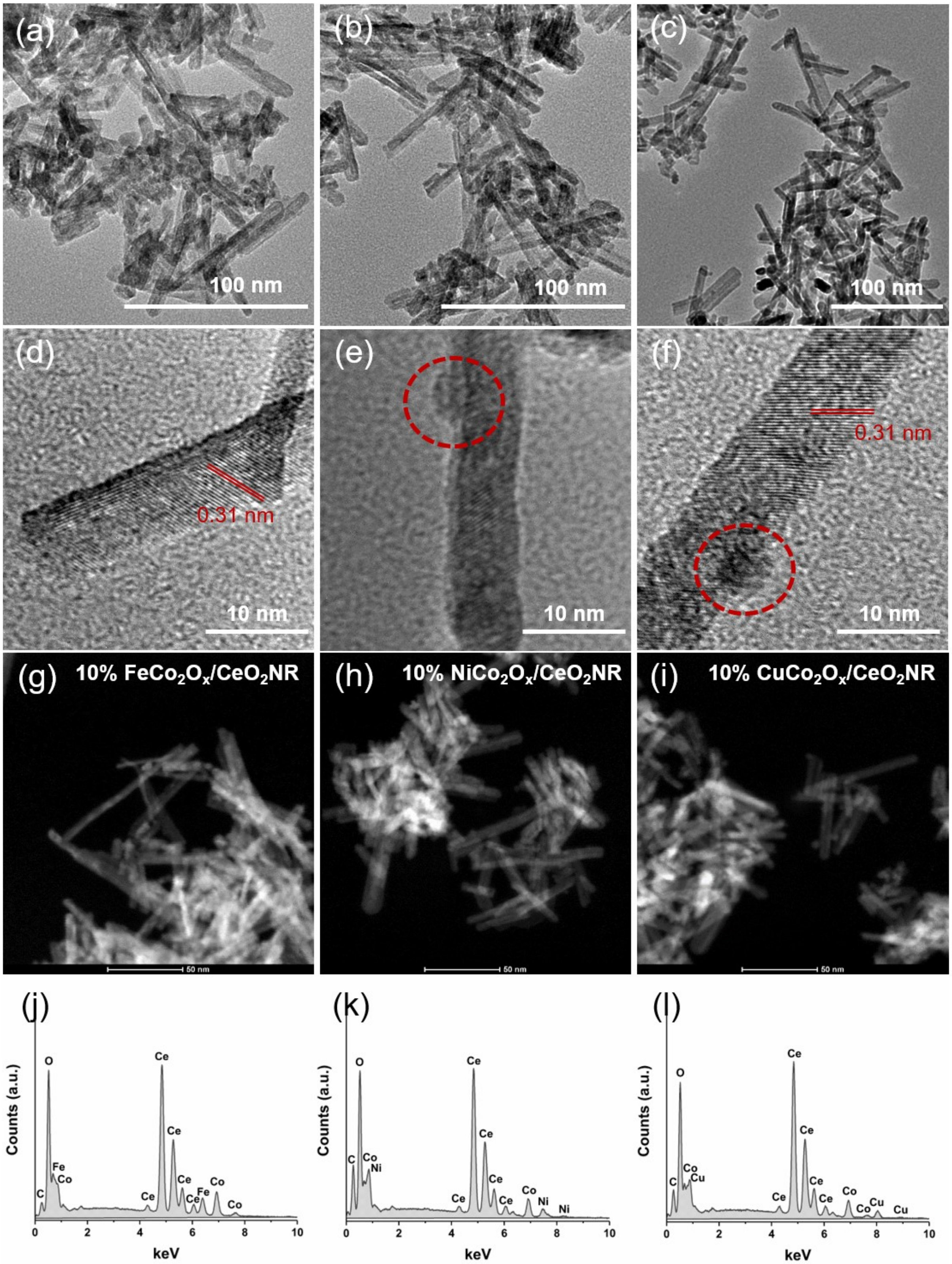

Figure 4. TEM (a-c), HRTEM (d-f), HAADF-STEM (g-i) images and EDS spectra of CeO_2NR supported 10% MCo_2O_x (M=Fe, Ni and Cu) catalysts.

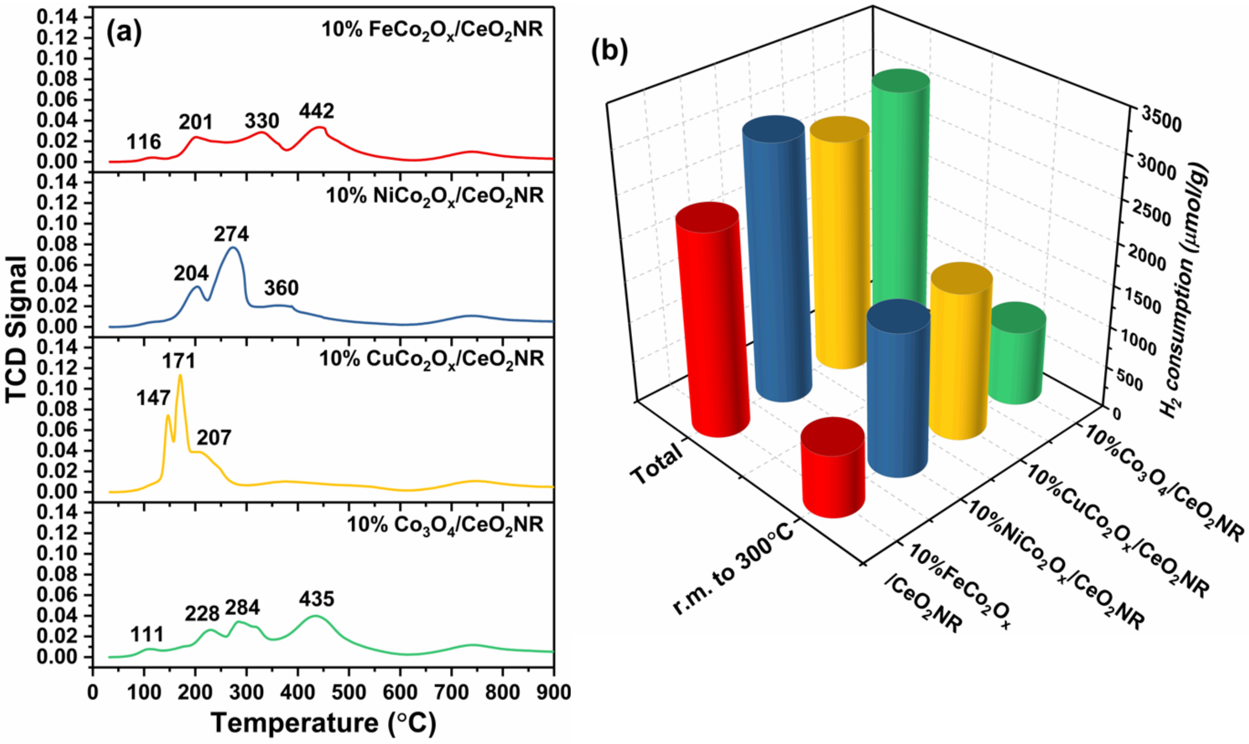

Figure 5. (a) H_2-TPR and (b) H_2 consumption (up to 300 °C and total) profiles of CeO_2NR supported Co_3O_4 and MCo_2O_x (M=Fe, Ni and Cu) catalysts.

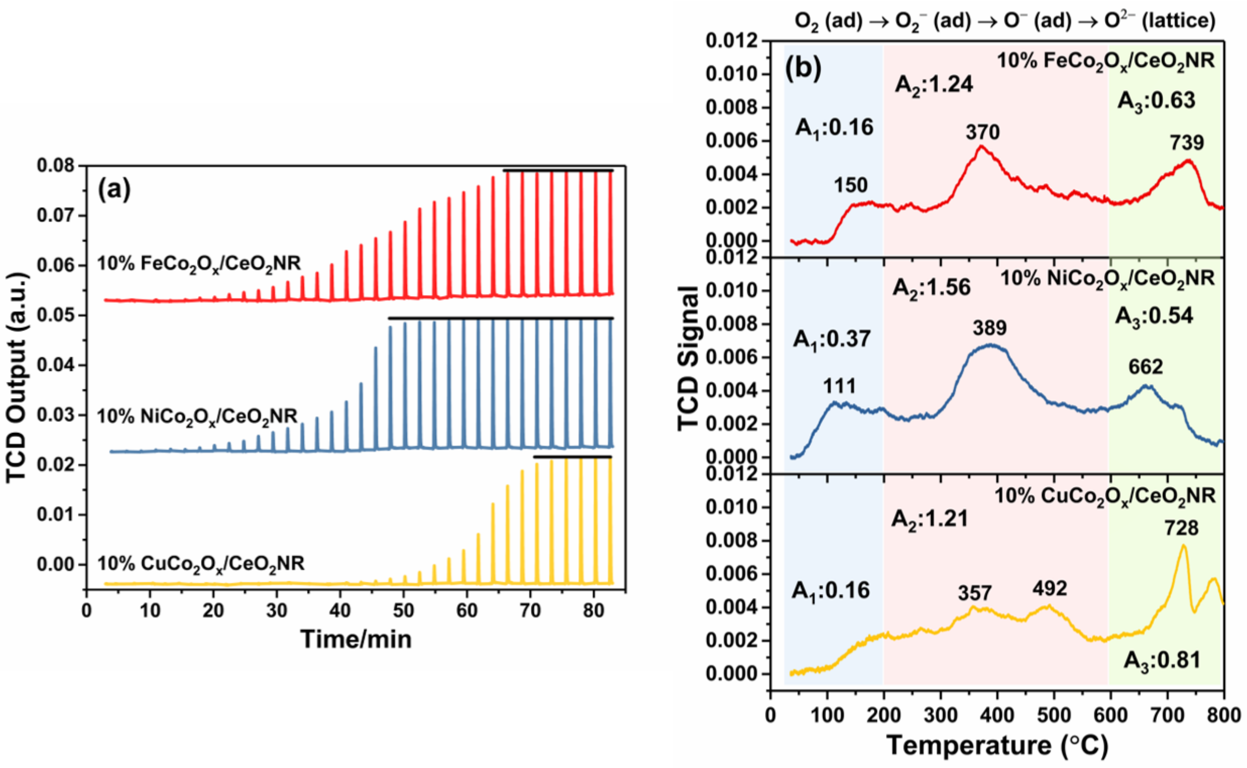

Figure 6. (a) O_2 pulse testing and (b) O_2-TPD over CeO$_2$NR supported MCo$_2$O$_x$ (M=Fe, Ni and Cu) catalysts.

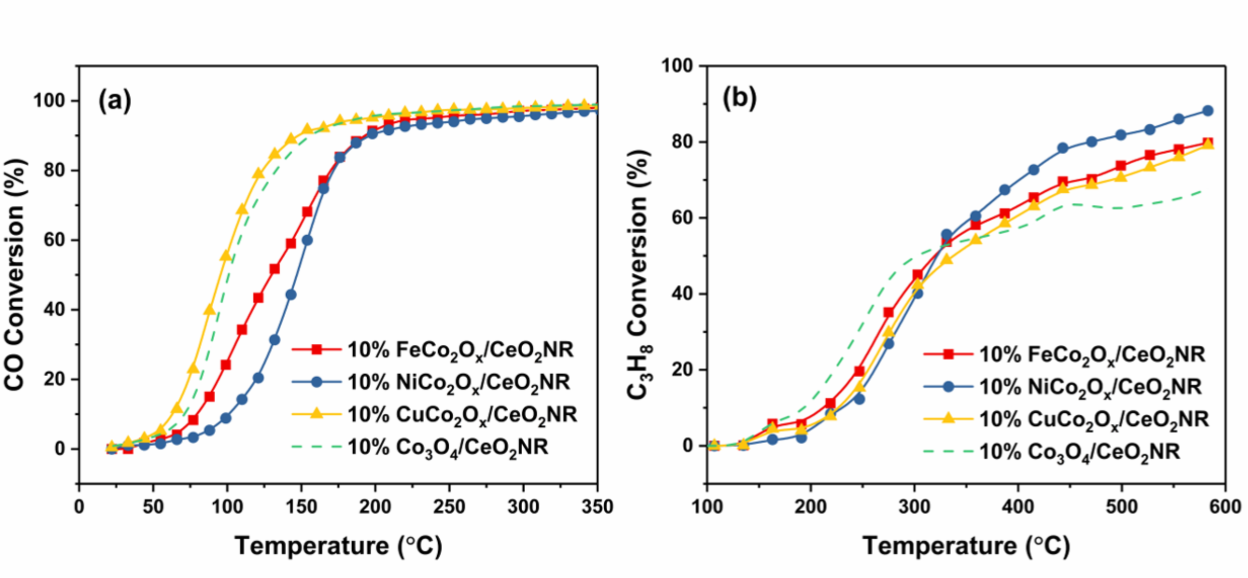

Figure 7. (a) CO oxidation light-off curves (1 vol.% CO/20 vol.% O_2/79 vol% He, GHSV: 46,000 mL h^{-1} $gcat^{-1}$) and (b) C_3H_8 oxidation light-off curves (0.2 vol% CO/2.0 vol.% O_2/97.8 vol% N_2, GHSV: 36,000 mL h^{-1} $gcat^{-1}$) over CeO_2NR supported MCo_2O_x (M=Fe, Ni and Cu) catalysts.

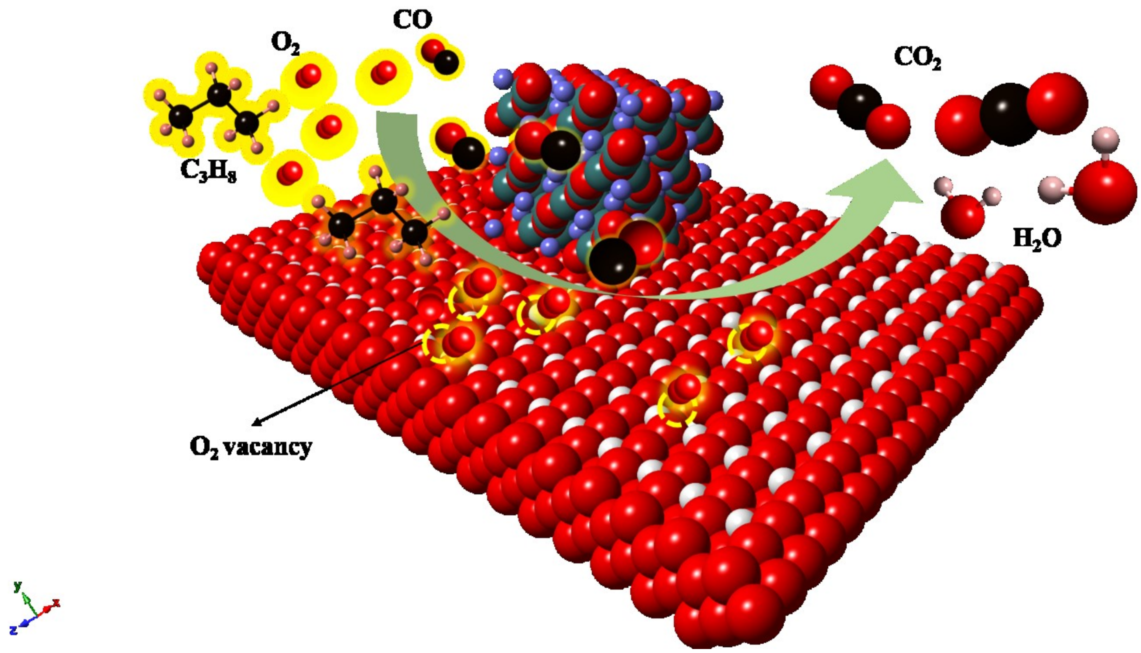

Figure 8. Reaction model of CO and C_3H_8 oxidation over CeO_2NR supported M–Co bimetallic oxide (M=Fe, Ni, Cu) catalysts.

Table 1. Co to M (M=Fe, Ni and Cu) ratio by EDS, BET surface area obtained from N_2-physisorption, crystallite size and lattice parameter calculated from XRD, and oxygen storage capacity.

Samples	**Co to M atomic ratio**	**S_{BET} (m^2/g)**	**Crystallite size of support[a] (nm)**	**a(Å)**	**OSCC (μmol O_2 $g_{cat.}^{-1}$)**
10% $FeCo_2O_x/CeO_2NR$	1.9	113.2	5.5	5.3871	468.2
10% $NiCo_2O_x/CeO_2NR$	2.0	108.6	5.5	5.3849	423.6
10% $CuCo_2O_x/CeO_2NR$	1.8	100.3	5.4	5.3882	641.0

[a] Estimated based on X-ray line broadening of the (111) reflection plane by Scherrer equation.

Table 2. Peak position of Raman Spectra.

Samples	**2TA**	**F_{2g}**	**D**
Pure CeO_2NR	246.3 cm^{-1}	456.0 cm^{-1}	594.9 cm^{-1}
10% $FeCo_2O_x/CeO_2$NR	239.9 cm^{-1}	443.3 cm^{-1}	560.4 cm^{-1} and 648.1 cm^{-1}
10% $NiCo_2O_x/CeO_2$NR	223.5 cm^{-1}	446.3 cm^{-1}	591.4 cm^{-1}
10% $CuCo_2O_x/CeO_2$NR	238.9 cm^{-1}	446.3 cm^{-1}	559.3 cm^{-1} and 646.4 cm^{-1}

Table 3. Reduction temperature ($\boldsymbol{T}_\mathbf{R}$) and H_2 consumption values of CeO_2NR supported MCo_2O_x (M=Fe, Ni and Cu) bimetallic catalysts (up to 300 °C and total).

Samples	T_R**(°C)**	**H_2 consumption (μmol/g)**	
		30 to 300 °C	**Total**
10% $FeCo_2O_x/CeO_2$NR	116, 201, 330, 442	755.7	2442.7
10% $NiCo_2O_x/CeO_2$NR	204, 274, 360	1725.4	3086.7
10% $CuCo_2O_x/CeO_2$NR	147, 171, 207	1772.6	2781.9
10% Co_3O_4/CeO_2NR	111, 228, 284, 435	907.5	3043.6

GRAPHIC ABSTRACT